Coupled aerostructural shape and topology optimization of horizontal-axis wind turbine rotor blades

Energy Conversion and Management 212 (2020) 112621

Contents lists available at ScienceDirect

Energy Conversion and Management

journal homepage: www.elsevier.com/locate/enconman

Coupled aerostructural shape and topology optimization of horizontal-axis wind turbine rotor blades

Zhijun Wang[a], Akke S.J. Suiker[a,*], Hèrm Hofmeyer[a], Twan van Hooff[a,b], Bert Blocken[a,b]

[a] Department of the Built Environment, Eindhoven University of Technology, P.O. Box 513, 5600 MB Eindhoven, The Netherlands
[b] Department of Civil Engineering, KU Leuven, Kasteelpark Arenberg 40 – Bus 2447, 3001 Leuven, Belgium

ARTICLE INFO

Keywords:
Wind turbine blade
Aerostructural design
Shape optimization
Topology optimization
Multi-objective optimization

ABSTRACT

Traditionally, Aerodynamic Shape Optimization (ASO) and Structural Topology Optimization (STO) are considered as two separate, consecutive stages in the aerostructural design process of wind turbine rotor blades. Since such a modeling strategy does not adequately account for the coupling effects between the blade aerodynamics and its structural performance, in this paper a Coupled Multi-objective Shape and Topology Optimization (CMSTO) approach is presented, which simultaneously optimizes the outer shape and the interior structural layout of the turbine blade from aerodynamic and structural requirements. The framework uses the weighted sum method, whereby the sum of the aerodynamic and structural objectives multiplied by specific weighting factors is minimized employing an incremental-iterative update procedure. The coupled optimization process is performed by sequentially carrying out shape and topology optimization steps for beam-type structures, in accordance with a staggered scheme. For the aerodynamic and structural optimizations the rotor power coefficient and the blade structural compliance are considered as the objectives, respectively. The aerodynamic response of the blade is evaluated by the Blade Element Momentum (BEM) method, which, together with a reduced beam-type Finite Element Method (FEM) model that simulates the structural response, facilitates the application of a gradient-based algorithm with analytical sensitivities. Accordingly, the computational efficiency of the CMSTO framework is warranted. The shape design variables are characterized by the locations of Non-Uniform Rational B-Splines (NURBS) control points that parameterize the blade outer shape. The topology design variables are represented by the relative densities assigned to the finite elements modeling the blade cross-sections, in correspondence with the Simplified Isotropic Material with Penalization (SIMP) method. The CMSTO framework is used to optimize the NREL 5 MW reference rotor blade, whereby the results are compared to those obtained from a separate ASO-STO approach and a pure STO approach. The rotor power coefficients calculated by the CMSTO and ASO-STO approaches are about 4% larger than that of the reference rotor blade. In addition, the blade structural compliance computed by the CMSTO approach is reduced by an extra 16% and 41% compared to the compliances found by ASO-STO and pure STO approaches, respectively. Such significant improvements clearly demonstrate the benefits of the CMSTO approach in the quest of wind turbines with higher power output and better structural performance.

1. Introduction

Over the past decades the optimization of the aerostructural performance of Horizontal-Axis Wind Turbines (HAWTs) has been an important subject of investigation [1], whereby the main challenge has been to design turbine blades characterized by i) a high power output, ii) a high stiffness, and iii) a low mass. These three objectives typically are conflicting: Maximizing the power output of turbine blades commonly results in an increase of the blade mass [2,3] and an increase of the aerodynamic loads [4]. Consequently, the structural deformation of the blade increases [5], which in turn puts more stringent requirements on its effective stiffness. Additionally, the use of a low amount of material opposes a high structural stiffness when the internal material distribution (i.e., the structural layout) of the blade is kept fixed [6,7].

The optimization of the aerostructural performance of wind turbines is usually carried out in two consecutive stages [8], which correspond to the aerodynamic design of the blade outer shape and the structural design of the interior layout of the blade. During the first stage, a shape optimization process is performed, in which the blade length, airfoil profile and chord and twist distributions of the blade are varied to

* Corresponding author.
E-mail address: A.S.J.Suiker@tue.nl (A.S.J. Suiker).

https://doi.org/10.1016/j.enconman.2020.112621
Received 20 November 2019; Received in revised form 14 February 2020; Accepted 16 February 2020

achieve an optimal aerodynamic performance [9–12]. The aerodynamic loads acting on the rotor can be calculated via Computational Fluid Dynamics (CFD) simulations or via the Blade Element Momentum (BEM) method [13]. Although CFD models provide an accurate representation of the complex aerodynamics of wind turbine blades [14–16], the high computational costs involved still withhold their incorporation in optimization frameworks [17]. During the second stage, the interior layout of the blade is optimized using the aerodynamic loads from the first stage as input. Traditionally, the optimization process starts from a hollow airfoil, whereby subsequently reinforcements (spar caps and shear webs) are added to improve the bending, shear, and torsional resistances of the blade [18]. The internal blade layout is usually optimized by adapting the thickness of the airfoil and the size and location of the reinforcements via size and shape optimization methods [19–21]. However, this strategy does not naturally allow for the introduction of new topological concepts for the blade layout, which is the reason that topology optimization techniques were introduced to find the optimal shapes and locations for the stiffeners of the turbine blades [22].

Since the shape and topology optimization processes typically are performed in two consecutive stages, the coupling effects between the blade aerodynamics and its structural performance are not adequately taken into account. The aerostructural design and multi-objective optimization techniques presented in [5,23–26] could overcome this limitation, but these frameworks so far have only been applied to specific blade layouts for which the outer shape is optimized together with the size and location of the stiffeners. In addition, the update of the design variables for most of the optimization techniques is performed with gradient-free optimization algorithms, such as genetic algorithms [2–7,25,26]. These algorithms facilitate an easy and flexible numerical implementation [3] and the possibility of finding a global optimum, but may also exhibit a poor convergence behavior [2] and thus are computationally expensive, especially if the number of design variables is relatively large [27]. From these viewpoints, gradient-based optimization methods, for which the sensitivities are derived in analytical form, are preferable.

In accordance with the aforementioned state of the art and challenges for the aerostructural design of large wind turbine blades, the novelty of this paper concerns the development of a Coupled Multi-objective Shape and Topology Optimization (CMSTO) framework that is able to simultaneously optimize the outer shape and interior topological layout of wind turbine rotor blades from aerodynamic and structural requirements. The framework uses the weighted sum method [28], whereby the sum of the aerodynamic and structural objectives multiplied by specific weighting factors is minimized. The rotor blade is simulated as a 2.5D reduced beam-type structure [29]; the efficiency and accuracy of this beam model have been validated in [30] through an extensive comparison with 3D beam models. Non-Uniform Rational B-Splines (NURBS) [31] are employed to parametrically describe the blade outer shape, which not only guarantees the smoothness of the blade shape, but also enables an efficient control of the geometry using only a few control points. The aerodynamic response of the blade is evaluated by the BEM method, for which the analytic sensitivities of the aerodynamic parameters are reported in the literature [27,24,32] and the numerical code is available open source [32]. The combination of the BEM method with a reduced beam-type FEM model supports the use of a gradient-based algorithm with analytical sensitivities, as a result of which the computational efficiency of the present optimization framework is warranted. With the coupled optimization method proposed in this paper, a better trade-off between the blade aerodynamic and structural performances can be achieved, which will be demonstrated through a practical case study related to a NREL 5 MW reference rotor blade.

The paper is organized as follows. Section 2 outlines the coupled aerostructural shape and topology optimization framework. The solution strategy and the numerical setup for the aerostructural optimization of a NREL 5 MW reference rotor blade are described in Section 3, and the numerical results are presented in Section 4. Finally, Section 5 summarizes the main conclusions of the optimization study.

2. Coupled aerostructural optimization model

In this section a Coupled Multi-objective Shape and Topology Optimization (CMSTO) model is presented that can be used for the aerostructural design of wind turbine blades. The model uses the weighted sum method [28], whereby the sum of the aerodynamic and structural objectives multiplied by specific weighting factors is minimized using an incremental-iterative numerical update procedure. The coupled optimization process is performed by sequentially carrying out shape and topology optimization steps for a beam-type structure, in accordance with the staggered scheme recently presented in previous works [30,33]. For the aerodynamic and structural optimizations the rotor power coefficient and the blade structural compliance are considered as the objectives, respectively. The shape design variables are characterized by the locations of NURBS control points that parameterize the blade outer shape. The topology design variables are represented by the relative densities assigned to the finite elements modeling the blade cross-sections, in correspondence with the Simplified Isotropic Material with Penalization (SIMP) method [34]. Accordingly, the coupled aerostructural optimization problem can be formulated as

$$\begin{aligned} \min_{\mathbf{a},\boldsymbol{\rho}} \quad & f(\mathbf{a},\boldsymbol{\rho}) = \omega\frac{C_{\mathrm{p0}}}{C_{\mathrm{p}}(\mathbf{a})} + (1-\omega)\frac{c(\mathbf{a},\boldsymbol{\rho})}{c_0}, \\ \text{subject to} \quad & \frac{V(\mathbf{a},\boldsymbol{\rho})}{V_0} \leqslant f_{\mathrm{r}}, \\ & \mathbf{A}\mathbf{a} \leqslant \mathbf{b}, \\ & \frac{A_n(\mathbf{a},\boldsymbol{\rho})}{A_n^0(\mathbf{a})} \leqslant f_{\mathrm{r}}, \qquad n = 1,\ldots,N, \\ \text{with} \quad & 0 \leqslant \frac{a_s - l_s}{u_s - l_s} \leqslant 1, \quad s = 1,\ldots,S, \\ & 0 \leqslant \rho_{min} \leqslant \rho_e \leqslant 1, \; e = 1,\ldots,E, \end{aligned} \tag{1}$$

where the rotor power coefficient C_{p} and the blade structural compliance c are the two objectives of the objective function f. The objectives are weighted by a weighting factor ω, with $0 \leqslant \omega \leqslant 1$. Since the objectives have different units, they are normalized by their initial values C_{p0} and c_0. Further, $\mathbf{a}$ is the vector containing the normalized blade shape design variables a_s, with their lower and upper bounds given by l_s and u_s, respectively, and S representing the total number of shape design variables. The vector $\boldsymbol{\rho}$ contains the topology design variables, ρ_e is the relative density assigned to finite element e, E is the total number of finite elements, and ρ_{min} is the minimum element density (which needs to be non-zero in order to avoid a singular stiffness matrix). The parameters V and V_0 represent the total material volume and initial blade volume, respectively, with their maximum fraction a priori prescribed as f_{r}, which is used for determining the initial value of the density ρ_e of each element. The matrix $\mathbf{A}$ and vector $\mathbf{b}$ include the linear inequality constraints for the shape design variables $\mathbf{a}$. Moreover, A_n^0 refers to the area of a specific blade cross-section n, and A_n represents the total area of material distributed across this cross-section. The maximum ratio of A_n and A_n^0 is controlled by the prescribed fraction f_{r}, and N is the total number of blade cross-sections.

In the coupled optimization formulation summarized in Eq. (1), the structural compliance c is minimized together with the inverse of the power coefficient C_{p} for a given initial blade outer shape and wind conditions. The structural compliance c is defined by

$$c = \mathbf{f}^{\mathrm{T}}\mathbf{u}, \tag{2}$$

with $\mathbf{f}$ and $\mathbf{u}$ the global force and displacement vectors of the FEM model for the rotor blade, which are related as

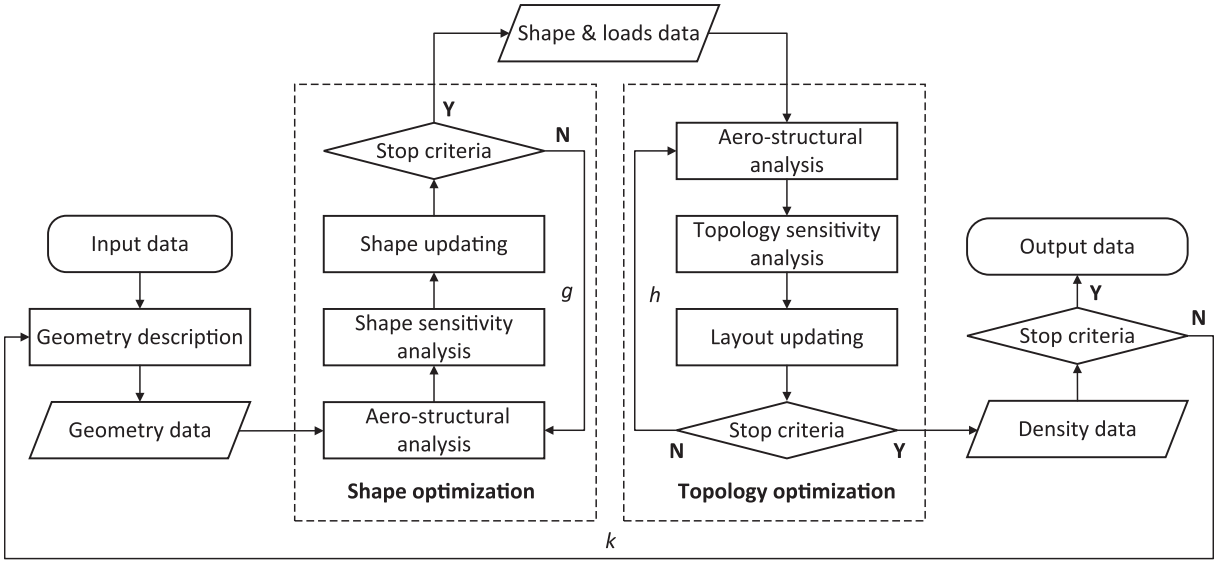

Fig. 1. Solution strategy for coupled shape and topology optimization. Iterations g and h refer to the shape and topology optimization sub-loops, respectively, and iteration k refers to the outer loop.

$$\mathbf{f} = \mathbf{K}\mathbf{u}, \tag{3}$$

where $\mathbf{K}$ is the overall stiffness matrix. Note that minimizing the inverse of the power coefficient is equivalent to maximizing the power coefficient. Similarly, minimizing the structural compliance c is equivalent to maximizing the overall stiffness of the rotor blade. Accordingly, by solving the coupled multi-objective optimization problem formulated by Eq. (1), a fixed amount of material can be optimally placed in a geometrically optimized design domain to achieve both a high rotor power coefficient and a high blade stiffness.

3. Numerical solution strategy

The coupled optimization problem formulated by Eq. (1) is solved numerically using a staggered scheme. As illustrated in Fig. 1, the blade outer shape and the structural layout are updated in an incremental-iterative fashion by alternatively performing shape and topology optimization steps. The formulation and numerical performance of this staggered scheme are presented in previous works, see [30,33].

In the numerical update scheme, first a multi-objective optimization step on the outer shape of the turbine blade is performed, formulated as

$$\begin{aligned} \min_{\mathbf{a}} \quad & f(\mathbf{a}) = \omega\frac{C_{\mathrm{p0}}}{C_{\mathrm{p}}(\mathbf{a})} + (1-\omega)\frac{c(\mathbf{a})}{c_0}, \\ \text{subject to} \quad & \frac{V(\mathbf{a})}{V_0} \leqslant f_{\mathrm{r}}, \\ & \mathbf{A}\mathbf{a} \leqslant \mathbf{b}, \\ & \frac{A_n(\mathbf{a})}{A_n^0(\mathbf{a})} \leqslant f_{\mathrm{r}}, \ n = 1,\ldots,N, \\ \text{with} \quad & 0 \leqslant \frac{a_s - l_s}{u_s - l_s} \leqslant 1, \ s = 1,\ldots,S, \end{aligned} \tag{4}$$

during which the element densities $\boldsymbol{\rho}$ are kept fixed. After Eq. (4) is solved, a topology optimization step is performed whereby the updated design variables $\mathbf{a}$ of the blade outer shape are temporarily kept fixed:

$$\begin{aligned} \min_{\boldsymbol{\rho}} \quad & f(\boldsymbol{\rho}) = \omega\frac{C_{\mathrm{p0}}}{C_{\mathrm{p}}} + (1-\omega)\frac{c(\boldsymbol{\rho})}{c_0}, \\ \text{subject to} \quad & \frac{V(\boldsymbol{\rho})}{V_0} \leqslant f_{\mathrm{r}}, \\ & \frac{A_n(\boldsymbol{\rho})}{A_n^0} \leqslant f_{\mathrm{r}}, \qquad n = 1,\ldots,N, \\ & 0 \leqslant \rho_{min} \leqslant \rho_e \leqslant 1, \ e = 1,\ldots,E. \end{aligned} \tag{5}$$

Note that the maximum value of the weighting factor ω in Eq. (5) should be smaller than 1 in order to carry out the topology optimization step. The optimized blade outer shape, obtained from solving Eq. (4), might not be structurally optimal anymore after the interior blade topology, represented by the element densities $\boldsymbol{\rho}$, has been optimized by solving Eq. (5). Correspondingly, the shape and topology optimization steps need to be alternately repeated until the stop criteria of the outer loop k are met, see Fig. 1. The details of the individual steps in the solution strategy are provided in the subsequent section by means of an illustrative example.

3.1. Geometry description

The features of the coupled optimization framework are

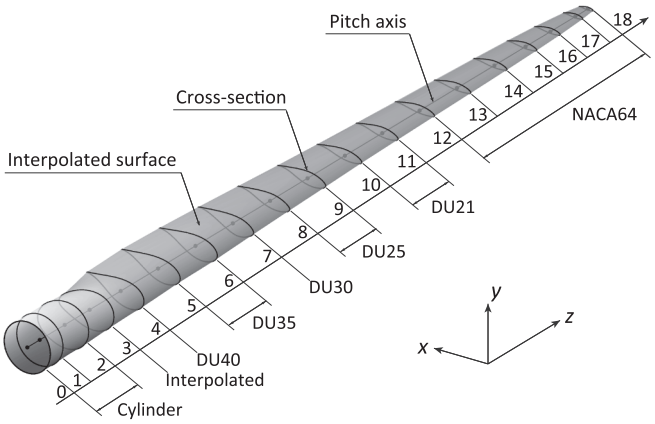

Fig. 2. Geometry of the NREL 5 MW reference wind turbine blade, constructed by 19 cross-sections, each related to a specific airfoil type. The specific cross-sections of the DU and NACA airfoil types are shown in Fig. 3.

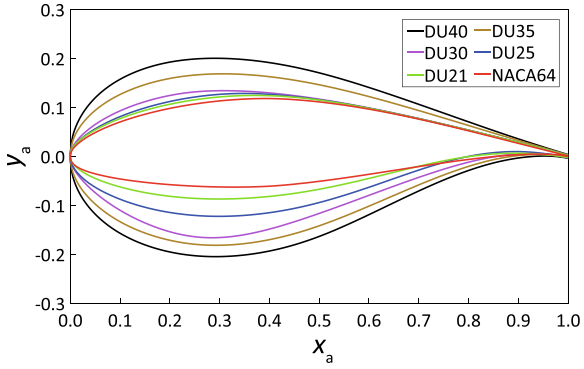

Fig. 3. Six airfoil types used for constructing the NREL 5 MW reference wind turbine blade, where DU and NACA refer to Delft University and National Advisory Committee for Aeronautics, respectively.

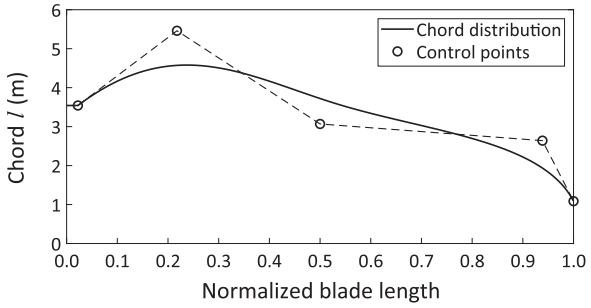

Fig. 4. Chord distribution along the blade length, described by NURBS with 5 control points. The circles indicate the initial locations of the control points.

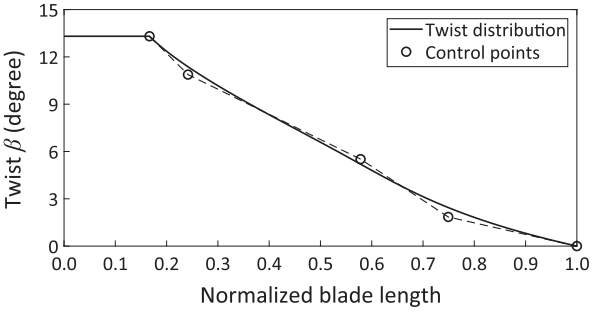

Fig. 5. Twist distribution along the blade length, described by NURBS with 5 control points. The circles indicate the initial locations of the control points.

demonstrated by selecting the National Renewable Energy Laboratory (NREL) 5 MW wind turbine rotor as a reference model, of which the design details are well documented in [35,36]. The blade geometry of the wind turbine rotor is described by 19 cross-sections along the blade length, see Fig. 2, with the geometry in between two adjacent cross-sections being determined by linear interpolation. The first two cross-sections near the blade root (i.e., cross-sections 0 and 1) are circular, in order to warrant a decent connection between the blade and the rotor. The blade reference geometry is constructed from the 6 airfoil types depicted in Fig. 3, whereby the geometry of each of these airfoil types is described by x- and y-coordinates that are normalized by the chord length l, i.e., $x_a = x/l$ and $y_a = y/l$. The final shape of the airfoil at each of the cross-sections is determined by upscaling the normalized shape presented in Fig. 3 using the actual chord length l, and subsequently rotating the airfoil in accordance with the corresponding twist angle β. The distributions of the chord length and twist angle along the blade length are plotted in Figs. 4 and 5, respectively, as taken from [35,36]. Each distribution was fitted by a NURBS curve equipped with 5 control points. The initial locations of the control points indicated in Figs. 4 and 5 were calculated such that the actual chord and twist distributions of the reference blade were accurately matched. In this way, the shape design variables $\mathbf{a}$ of the blade are fully determined by the control point locations of the blade chord and twist distributions. During the optimization procedure the first control point (located close to the blade root) and last control point (located at the blade tip) of the chord and twist distributions are allowed to move only vertically, in correspondence with the assumption that the length of the blade remains constant. The other three control points can move both horizontally and vertically, but are not allowed to intersect or pass each other. Additionally, from general design considerations the blade chord distribution after the second control point is enforced to monotonically decrease towards the blade tip [3]. In other words, the chord lengths related to the second, third, fourth and fifth control points are required to successively decrease in value. More details on the use of NURBS for describing structural geometries can be found in [31,30] and references therein.

The above-described mapping from a normalized airfoil geometry to the actual blade cross-section is illustrated in Fig. 6, and can be described by means of a geometry function $\mathbf{G}$ given by

$$\mathbf{G}(\mathbf{p}_a) = l\mathbf{R}(\mathbf{p}_a - \mathbf{o}_c) + \mathbf{o}_b. \tag{6}$$

Here, $\mathbf{p}_a = [x_a, y_a]^T$ is an arbitrary point on the normalized airfoil geometry, $\mathbf{o}_c = [x_0, y_0]^T$ is the location of the origin of the normalized airfoil geometry, which is chosen to correspond to the blade pitch axis, see Fig. 2, with the locations of the pitch axis of the 6 airfoil types depicted in Fig. 3 taken from [37]. Further, $\mathbf{o}_b = [x_b, y_b]^T$ represents the location of the origin of the actual cross-section (=blade pitch axis), which for simplicity is defined as $\mathbf{o}_b = [0, 0]^T$, l is the blade chord length

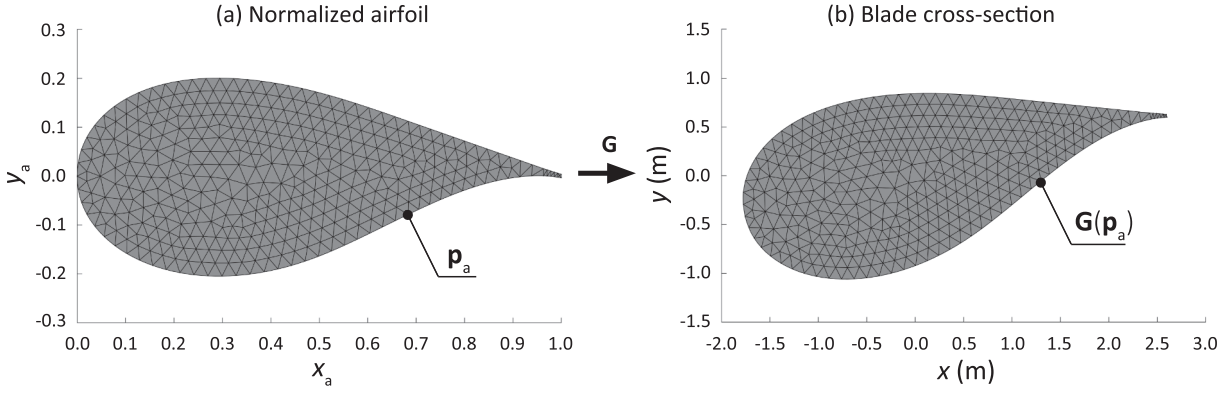

Fig. 6. Visualization of the geometrical mapping $\mathbf{G}$, given by Eq. (6), from a) a normalized airfoil geometry to b) a blade cross-section. The finite element discretization is designated by the solid lines.

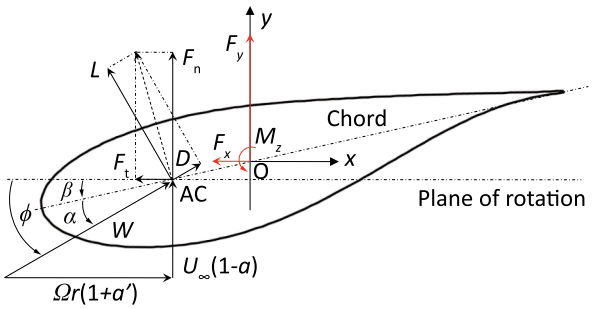

Fig. 7. Components of the velocity and the aerodynamic load at a cross-section of the rotor blade.

of the specific cross-section, as defined in Fig. 4, and **R** is the rotation matrix, given by

$$\mathbf{R} = \begin{bmatrix} \cos\beta & -\sin\beta \\ \sin\beta & \cos\beta \end{bmatrix}, \tag{7}$$

with β the blade twist angle of the actual cross-section, as defined in Fig. 5.

The blade cross-sections are discretized by finite elements in order to compute the interior layout of the blade by density-based topology optimization. The mesh of a cross-section is obtained by mapping a predefined finite element mesh for the normalized airfoil using the geometry function **G** given by Eq. (6). With this procedure, the number of elements, which equals the number of topology design variables $\boldsymbol{\rho}$, is kept fixed for each cross-section during the optimization procedure. Note that cross-sections based on the same airfoil type, such as cross-sections 12 to 18 shown in Fig. 2, have the same finite element mesh. Accordingly, in order to reduce the computational demand of the optimization procedure, cross-sections with the same finite element mesh are assigned the same set of topology optimization variables $\boldsymbol{\rho}$. Further, the discretization strategy naturally enables the computation of analytical derivatives of the nodal coordinates with respect to the shape design variables $\boldsymbol{a}$, as required for gradient-based optimization.

3.2. Aerostructural analysis

3.2.1. Aerodynamic analysis

For the aerodynamic analysis of the HAWT reference rotor, the BEM method [38] is adopted. This method is reviewed below, and its application towards the aerodynamic analysis of the reference turbine rotor is explained. The cross-section of a rotating turbine blade is illustrated in Fig. 7. As indicated in this figure, the local flow angle ϕ follows from the expression $\tan\phi = U_\infty(1-a)/(r\ \Omega(1+a'))$, whereby r is the radial location of the blade cross-section, Ω is the rotor rotational speed and U_∞ represents the free-stream wind speed. Further, a and a' are the axial and angular induction factors, respectively, which both are a function of the local flow angle ϕ, i.e., $a = \hat{a}(\phi)$ and $a' = \hat{a}'(\phi)$, see [38] for the specific forms. The above expression can be simply reformulated as

$$f(\phi) = \frac{\sin\phi}{1-a} - \frac{\cos\phi}{\lambda_r(1+a')} = 0, \tag{8}$$

where the parameter $\lambda_r = r\ \Omega/U_\infty$ is commonly referred to as the local tip-speed ratio. Eq. (8) can be solved iteratively for ϕ using a one-dimensional root-finding algorithm, such as Brent's method [38]. Once the local inflow angle ϕ is determined, the induced aerodynamic normal and tangential forces F_n and F_t acting on the blade cross-section, see Fig. 7, can be calculated in accordance with the procedure illustrated by the flowchart in Fig. 8. The flowchart starts with the computation of the local angle of attack α and the local Reynolds number Re, using the value of the local flow angle ϕ resulting from Eq. (8). As illustrated in Fig. 7, the angle of attack follows from the expression

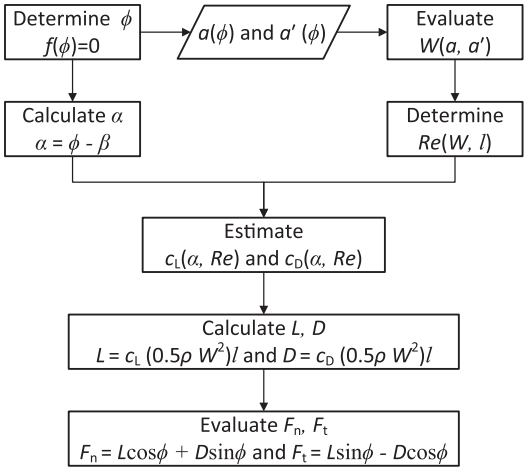

Fig. 8. Flow chart for the calculation of the aerodynamic forces acting on the blade cross-section.

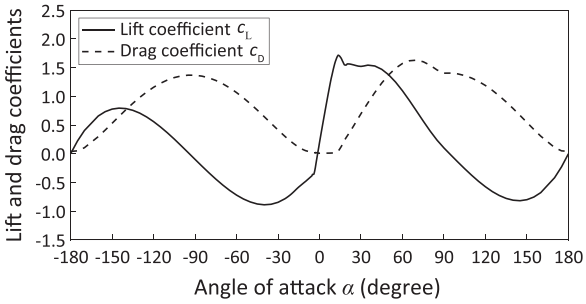

Fig. 9. Lift and drag coefficients for a DU35 airfoil as a function of the angle of attack, using a Reynold's number $Re = 1 \times 10^6$.

$\alpha = \phi - \beta$, where β is the twist angle, with its distribution along the blade length given in Fig. 5. The local Reynolds number is computed by inserting the values for the axial and angular induction factors, $a = \hat{a}(\phi)$ and $a' = \hat{a}'(\phi)$, into the expression for the local inflow velocity, which, in accordance with Fig. 7, is given by $W = \sqrt{U_\infty^2(1-a)^2 + (r\ \Omega)^2(1+a')^2}$. Subsequently, the resulting value of W is used together with the chord length l for computing the local Reynolds number as $Re = \rho W l/\mu$, where $\rho = 1.225\,\mathrm{kg/m^3}$ and $\mu = 1.812 \times 10^{-5}\,\mathrm{Ns/m^2}$ represent the density and dynamic viscosity of air, respectively. With the specific angle of attack α and local Reynolds number Re being calculated, the lift coefficient c_L and drag coefficient c_D can be computed from the data tabulated in [35]. Fig. 9 illustrates a specific example of these data, which is related to a DU35 airfoil at a Reynolds number $Re = 1 \times 10^6$. From the lift and drag coefficients, the lift force L and drag force D can be computed using the expressions $L = c_L\rho W^2 l/2$ and $D = c_D\rho W^2 l/2$, respectively, see also Figs. 7 and 8. Finally, the forces F_n and F_t normal and tangential to the plane of rotation can be calculated from the lift force L and drag force D via $F_n = L\cos\phi + D\sin\phi$ and $F_t = L\sin\phi - D\cos\phi$, see also Fig. 7. To apply the aerodynamic forces on the FEM model for the rotor blade, the normal force F_n and tangential force F_t need to be transferred from the aerodynamic center AC to the reference point O (=pitch axis), as shown in Fig. 7. This transformation result in the following aerodynamic loads:

$$\begin{cases} F_x = F_t, \quad F_y = F_n, \\ M_z = -d(F_t\sin\beta + F_n\cos\beta), \end{cases} \tag{9}$$

where d is the distance between the aerodynamic center AC and the reference point O and M_z is a torsional moment about point O. Finally, the forces F_x, F_y and M_z at each blade cross-section are used to construct the global load vector **f** used for solving the structural equilibrium of

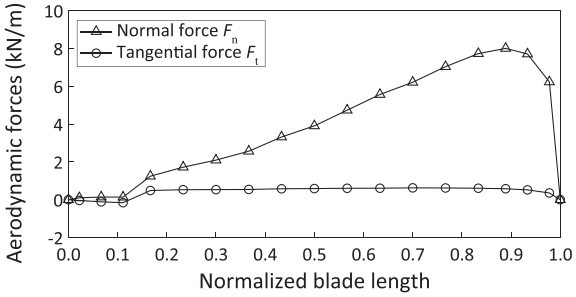

Fig. 10. Distribution of the normal and tangential aerodynamic forces along the blade length.

the turbine blade, see Eq. (3).

Setting the free-stream wind speed as $U_\infty = 10\,\mathrm{m/s}$ and the blade tip-speed ratio as $\lambda_r = 9$, the distribution of the aerodynamic loads on the blade naturally follows from the normal and tangential forces at the cross-sections along the blade, as depicted in Fig. 2. For the parameters indicated above the result is depicted in Fig. 10. Note that the tangential force distribution can be used to calculate the torque generated on the rotor shaft [39], which in turn can be employed to calculate the power coefficient C_p of the rotor. As indicated by Eq. (1), during the optimization procedure the rotor power coefficient C_p is maximized under the given aerodynamic loading conditions. More specific details on the BEM method can be found in [38,40]. In the current work an existing implementation of the BEM method has been used, as provided via the open source software CCBlade, see [32] for background information.

3.2.2. Structural analysis

The structural response of the turbine blade to the aerodynamic loads is calculated by means of an FEM analysis. The turbine blade is discretized as a 2.5D beam-type structure, which is a model whereby the response of a relatively long and slender structure, such as plotted in Fig. 11(a), is evaluated by a reduced beam-type FEM configuration shown in Fig. 11(c), instead of a full 3D FEM configuration sketched in Fig. 11(b). Specifically, the 2.5D beam-type FEM model simulates the longitudinal direction of the turbine blade by elementary beam elements, for which the properties at specific cross-sections are determined from corresponding 2D continuum element models, see [29,30] for more details on this modeling approach. In the present work the cross-sections analyzed with a 2D continuum element model coincide with the cross-sections used for modeling the turbine blade, see Fig. 2, which allows to straightforwardly impose the aerodynamic loading calculated with the BEM method on the turbine blade.

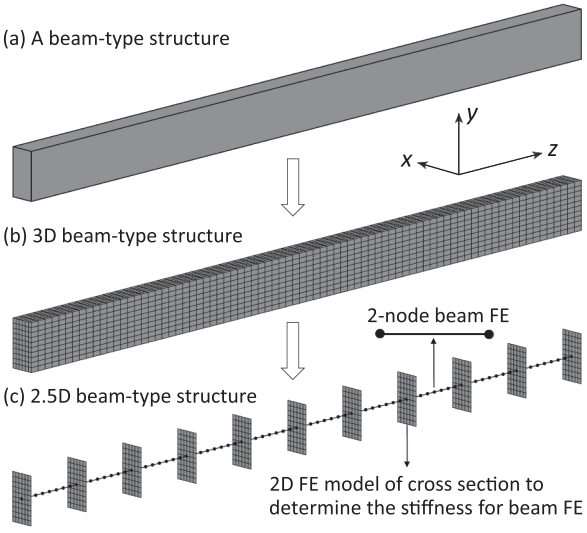

Fig. 11. FEM discretization. Example of (a) a relative slender beam structure, modeled as (b) a 3D configuration, and (c) a 2.5D configuration.

The specific stiffness $\mathbf{K}^s$ of a blade cross-section is dependent on its outer shape and its internal topology via the shape design variables $\mathbf{a}$ and the topology design variables $\boldsymbol{\rho}$. The relative densities representing the topology design variables are evaluated at the individual elements e modeling the 2D cross-section, $\boldsymbol{\rho} = \rho_e$, and determine the Young's modulus of the element in accordance with the SIMP (Simplified Isotropic Material with Penalization) approach as [34]

$$E_e(\rho_e) = \rho_e^p E_0. \tag{10}$$

Here, p is a penalization factor, a typical value being 3 [34], and E_0 is the initial Young's modulus of the material. From the cross-sectional stiffness $\mathbf{K}^s$ the beam element stiffness $\mathbf{k}^b$ can be constructed, see [29,30], which, after the element assemblage procedure, provides the global stiffness matrix $\mathbf{K}$ at the structural level. The load vector $\mathbf{f}$ at the structural level is characterized by the aerodynamic forces calculated with the BEM method, as described in Section 3.2.1. With the stiffness $\mathbf{K} = \mathbf{K}(\mathbf{a}, \boldsymbol{\rho})$ and load vector $\mathbf{f} = \mathbf{f}(\mathbf{a})$ being characterized, the overall structural compliance c can be calculated by inserting Eq. (3) into Eq. (2), which results in

$$c = \mathbf{f}^{\mathrm{T}}(\mathbf{a})\mathbf{K}^{-1}(\mathbf{a}, \boldsymbol{\rho})\mathbf{f}(\mathbf{a}). \tag{11}$$

In order to perform the optimization process in a computationally efficient manner, a gradient-based method is adopted for which the derivatives of the structural compliance c with respect to the shape variables $\mathbf{a}$ and topology variables $\boldsymbol{\rho}$ are computed analytically, see Section 3.3 below.

3.3. Sensitivity analysis

3.3.1. Shape sensitivity

As demonstrated in Section 3.2.1, the aerodynamic forces F_n and F_t are determined by the geometry of the blade cross-section. In correspondence with Fig. 6, the geometry of a blade cross-section is parameterized by the geometry function $\mathbf{G}$ given by Eq. (6), which depends on the chord length l and the twist angle β of the blade, see also Eq. (7), with their distributions along the blade length presented in Figs. 4 and 5, respectively. Hence, the derivatives of the aerodynamic forces $\mathbf{F} = [F_\mathrm{n}, F_\mathrm{t}]^{\mathrm{T}}$ with respect to the shape design variables $\mathbf{a}$ (i.e., the coordinates of the NURBS control points) are calculated by applying the chain rule

$$\frac{\partial \mathbf{F}}{\partial a_s} = \frac{\partial \mathbf{F}}{\partial l}\frac{\partial l}{\partial a_s} + \frac{\partial \mathbf{F}}{\partial \beta}\frac{\partial \beta}{\partial a_s}, \tag{12}$$

in which a_s refers to a specific element in the vector of shape design variables $\mathbf{a}$. The analytical derivatives of the aerodynamic forces with respect to the chord length $\partial\mathbf{F}/\partial l$ and twist angle $\partial\mathbf{F}/\partial\beta$ are provided by the program CCBlade [32]. In addition, analytical expressions for $\partial l/\partial a_s$ and $\partial\beta/\partial a_s$ can be calculated using NURBS theory [31,30]. Eq. (12) is subsequently substituted into the derivatives of the aerodynamic loads with respect to the shape variables a_s, which from Eq. (9) follow as

$$\begin{cases} \dfrac{\partial F_\mathrm{x}}{\partial a_s} = \dfrac{\partial F_\mathrm{t}}{\partial a_s}, \\ \dfrac{\partial F_\mathrm{y}}{\partial a_s} = \dfrac{\partial F_\mathrm{n}}{\partial a_s}, \\ \dfrac{\partial M_\mathrm{z}}{\partial a_s} = -\dfrac{\partial d}{\partial a_s}(F_\mathrm{t}\sin\beta + F_\mathrm{n}\cos\beta) \\ \qquad\qquad - d\left(\dfrac{\partial F_\mathrm{t}}{\partial a_s}\sin\beta + F_\mathrm{t}\cos\beta\dfrac{\partial \beta}{\partial a_s}\right. \\ \qquad\qquad\quad \left. + \dfrac{\partial F_\mathrm{n}}{\partial a_s}\cos\beta - F_\mathrm{n}\sin\beta\dfrac{\partial \beta}{\partial a_s}\right). \end{cases} \tag{13}$$

Note that the derivative $\partial d/\partial a_s = 0$ when a_s is related to the blade twist angle β, since the distance d between the aerodynamic center AC and the reference point O is set by the blade chord l.

In accordance with the construction of the FEM mesh of a blade cross-section depicted in Fig. 6, the derivatives of the location of an arbitrary element node $\mathbf{p} = \mathbf{G}(\mathbf{p}_a) = [x, y]^T$ with respect to the element shape design variable a_s are obtained from Eq. (6) as

$$\frac{\partial \mathbf{p}}{\partial a_s} = \frac{\partial \mathbf{G}(\mathbf{p}_a)}{\partial a_s} = \frac{\partial \mathbf{G}(\mathbf{p}_a)}{\partial l}\frac{\partial l}{\partial a_s} + \frac{\partial \mathbf{G}(\mathbf{p}_a)}{\partial \beta}\frac{\partial \beta}{\partial a_s}, \tag{14}$$

with

$$\frac{\partial \mathbf{G}(\mathbf{p}_a)}{\partial l} = \mathbf{R}(\mathbf{p}_a - \mathbf{o}_c), \quad \frac{\partial \mathbf{G}(\mathbf{p}_a)}{\partial \beta} = l\frac{\partial \mathbf{R}}{\partial \beta}(\mathbf{p}_a - \mathbf{o}_c), \tag{15}$$

where $\mathbf{p}_a$ represents the location of the node in the mesh of the normalized airfoil profile, see Fig. 6, $\partial \mathbf{R}/\partial \beta$ can be calculated from Eq. (7), and $\partial l/\partial a_s$ and $\partial \beta/\partial a_s$ can be obtained as described below Eq. (12). Finally, the derivative of the structural compliance c with respect to the shape design variable a_s follows from Eq. (11) as

$$\frac{\partial c}{\partial a_s} = \frac{\partial \mathbf{f}^T}{\partial a_s}\mathbf{K}^{-1}\mathbf{f} + \mathbf{f}^T\frac{\partial \mathbf{K}^{-1}}{\partial a_s}\mathbf{f} + \mathbf{f}^T\mathbf{K}^{-1}\frac{\partial \mathbf{f}}{\partial a_s}, \tag{16}$$

whereby the applied aerodynamic loads $\mathbf{f}$ and their shape sensitivities $\partial \mathbf{f}/\partial a_s$ are given by Eqs. (9) and (13), respectively. Furthermore, the shape sensitivities of $\mathbf{K}^{-1}$ are calculated as $\partial \mathbf{K}^{-1}/\partial a_s = -\mathbf{K}^{-1}(\partial \mathbf{K}/\partial a_s)\mathbf{K}^{-1}$, where $\partial \mathbf{K}/\partial a_s$ follows the formulation given in [30]. The derivatives of the objective function with respect to the shape variables are obtained from Eq. (4) as

$$\frac{\partial f}{\partial a_s} = -\frac{\omega C_{p0}}{(C_p)^2}\frac{\partial C_p}{\partial a_s} + \frac{1-\omega}{c_0}\frac{\partial c}{\partial a_s}, \tag{17}$$

with

$$\frac{\partial C_p}{\partial a_s} = \frac{\partial C_p}{\partial l}\frac{\partial l}{\partial a_s} + \frac{\partial C_p}{\partial \beta}\frac{\partial \beta}{\partial a_s}, \tag{18}$$

where $\partial c/\partial a_s$ is given by Eq. (16), the rotor power coefficient C_p and its derivatives with respect to the chord length, $\partial C_p/\partial l$, and twist, $\partial C_p/\partial \beta$, are obtained from the program CCBlade [32], and $\partial l/\partial a_s$ and $\partial \beta/\partial a_s$ are derived as described below Eq. (12).

3.3.2. Topology sensitivity

The derivative of the structural compliance c with respect to the relative density ρ_e in a finite element is obtained from Eqs. (2) and (3) as

$$\frac{\partial c}{\partial \rho_e} = -\mathbf{u}^T\frac{\partial \mathbf{K}}{\partial \rho_e}\mathbf{u}, \tag{19}$$

which uses the assumption that the aerodynamic load vector $\mathbf{f}$ is independent of the element relative densities $\boldsymbol{\rho}$, see also Eq. (11). The specific form of $\partial \mathbf{K}/\partial \rho_e$ is taken from [30]. To alleviate possible checkerboard patterns in the spatial distributions of the element relative densities, a sensitivity filter is introduced [41]

$$\frac{\partial \hat{c}}{\partial \rho_e} = \frac{1}{\rho_e \sum_{f=1}^{N} \hat{H}_f}\sum_{f=1}^{N} \hat{H}_f \rho_f \frac{\partial c}{\partial \rho_f}, \tag{20}$$

in which $\partial c/\rho_f$ is calculated using Eq. (19), $\widehat{H}_f = \max(0, r_{\min} - \mathrm{dist}(e, f))$, where $\mathrm{dist}(e, f)$ is the distance between the center of finite element e and the center of element f, and $r_{\min}$ is the radius of the circle in which smoothing takes place. Due to the coupling with shape optimization, the element size during the optimization procedure is variable. Consequently, depending on the location and shape of elements, a constant filter radius may cause that multiple elements are filtered together. To avoid this situation, the radius of the filter is defined as $r_{min} = r_0\sqrt{V_e}$, where V_e is the area of element e, and r_0 is a predefined scaling parameter for the radius, which is set to 1.2.

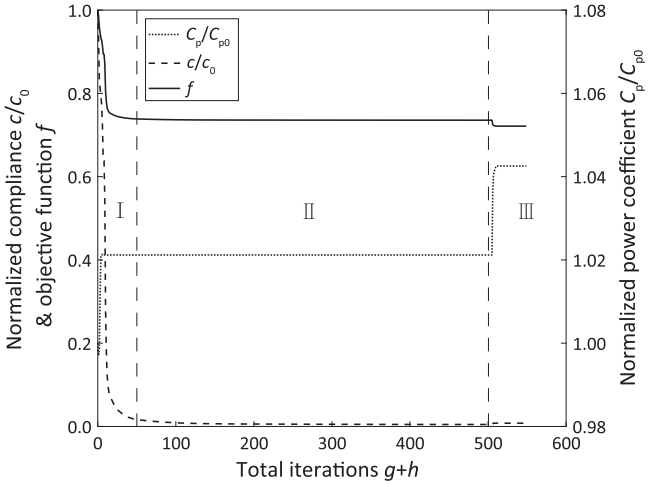

Fig. 12. Convergence behavior (divided in stages I, II and III) of the normalized compliance c/c_0, normalized power coefficient C_p/C_{p0} and objective function f, using the CMSTO approach with $\omega = 0.75$.

Finally, the derivative of the overall objective function in Eq. (5) with respect to the element density ρ_e can be formulated as

$$\frac{\partial f}{\partial \rho_e} = \frac{1-\omega}{c_0}\frac{\partial \hat{c}}{\partial \rho_e}, \tag{21}$$

with $\partial \hat{c}/\partial \rho_e$ given by Eq. (20).

4. Simulation results

In order to demonstrate the specific features of the CMSTO framework proposed here, the optimized blade designs following from this approach are compared against the results obtained by two other approaches, namely a separate Aerodynamic Shape Optimization and Structural Topology Optimization (ASO-STO) approach often used in blade design practice, and a pure Structural Topology Optimization (STO) approach. First, the CMSTO approach is applied. In the CMSTO framework, the weighting factor ω characterizing the objective function, see Eq. (1), is varied in order to determine whether the optimization should be biased towards the rotor power coefficient or to the blade structural compliance. For this purpose, five values were selected, which are $\omega = 0, 0.25, 0.50, 0.75, 0.99$. The maximum value of ω is set to 0.99 (instead of 1), to prevent that the coupled multi-objective optimization model reduces to a pure aerodynamic shape optimization model. Additionally, the maximal material volume fraction f_r in Eq. (1) is set to 0.125 in accordance with [22], which thus warrants that the total material volume used for the blade should not be more than 12.5% of the initial blade volume. In the update procedure of the design variables the Sequential Quadratic Programming (SQP) method (implemented in the MATLAB *fmincon* solver) has been employed, which utilizes the analytical sensitivities presented in Section 3.3.

Fig. 12 shows the convergence behavior of the CMSTO approach for the normalized blade compliance c/c_0, the normalized rotor power coefficient C_p/C_{p0}, and the objective function f. Here, c_0 and C_{p0} are the initial values of the structural compliance of the blade and the power coefficient, respectively. The weighting factor used in the CMSTO approach equals $\omega = 0.75$. The iterations g and h, summed up along the horizontal axis, refer to the shape optimization and topology optimization sub-loops, respectively, see Fig. 1. In order to clarify the discussion of the results, the convergence behavior following from the alternating shape and topology optimization steps depicted in Fig. 12 has been divided into three stages, designated as stages I, II and III. The significant variations characterizing stages I and III are shown enlarged in Figs. 13 and 14, respectively. It can be seen from Fig. 13 that during

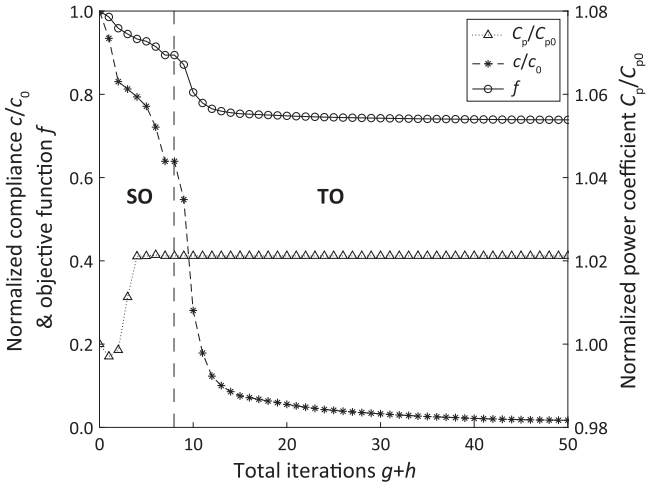

Fig. 13. Close-up of convergence stage I depicted in Fig. 12.

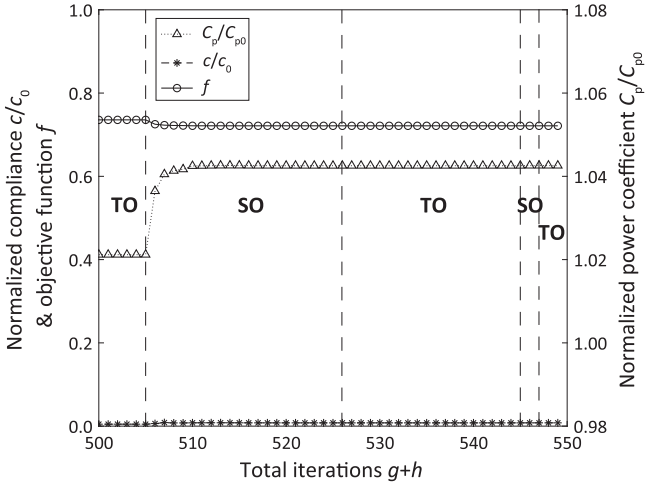

Fig. 14. Close-up view of convergence stage III depicted in Fig. 12.

the initial shape optimization (SO) step of stage I, which is performed in accordance with Eq. (4), the normalized power coefficient C_p/C_{p0} indeed increases and that the normalized compliance c/c_0 and the objective function f decrease with an increasing number of iterations. In the subsequent topology optimization (TO) step, c/c_0 and f continue to decrease with the number of iterations, due to a further optimization of the interior layout of the blade, see Eq. (5). The value of C_p/C_{p0} remains constant, since the blade outer shape is temporarily kept fixed. Note from stage II in Fig. 12 that for all three parameters the convergence behavior during this topology optimization step is relatively slow. In the final stage III, the normalized power coefficient C_p/C_{p0} again shows a substantial jump during the first shape optimization step, see Fig. 14. However, after performing two more topology optimization steps and one additional shape optimization step the iterative process has converged by satisfying the stop criterion, $|f^{k+1} - f^k| \leqslant$1e-5.

As illustrated in Fig. 15, for all five selected weighting factors ω the CMSTO approach is characterized by a robust convergence behavior of the objective function f. For $\omega > 0.50$ the total number of iterations appears to increase with increasing value of ω, such that for $\omega = 0.99$ the number of iterations is about 5.5 times larger than for $\omega = 0.50$ (note that the horizontal axis is scaled differently for $\omega = 0.99$).

Fig. 16 illustrates the normalized rotor power coefficient C_p/C_{p0} and normalized blade structural compliance c/c_0 calculated by the CMSTO approach for the 5 selected weight factors, $\omega = 0$, 0.25, 0.50, 0.75, 0.99, and 5 additional values, $\omega = 0.05$, 0.075, 0.10, 0.15, 0.20 (circles). The

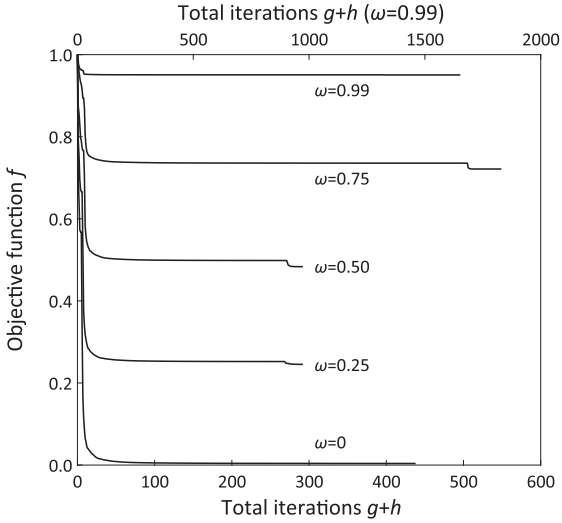

Fig. 15. Convergence behavior of the objective function f, using the CMSTO approach with different weighting factors ω.

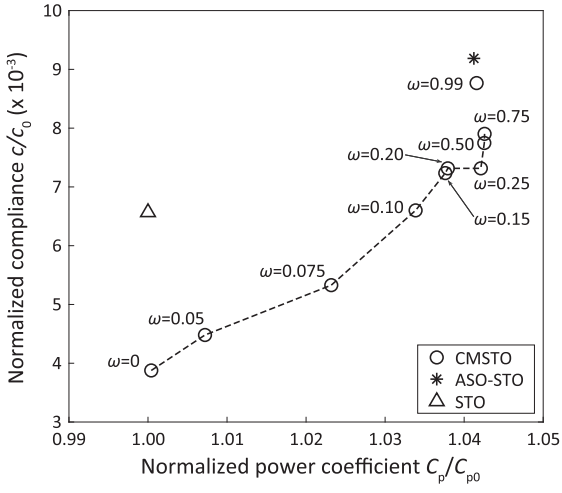

Fig. 16. Normalized rotor power coefficient C_p/C_{p0} and normalized blade structural compliance c/c_0 of the optimized designs calculated with three different optimization strategies (CMSTO (circles), ASO-STO (asterisk), STO (triangle)). The circles connected by the dashed line represent the Approximate Pareto Front (APF) constructed from the CMSTO results.

result is compared to that computed by the ASO-STO approach (asterisk) and the STO approach (triangle). In correspondence with [42], the non-dominated points computed by CMSTO approach, which are connected by the dashed line, determine a so-called Approximate Pareto Front (APF). Along the APF, which is represented by weighting factors in the range $0 \leqslant \omega \leqslant 0.75$, both the normalized power coefficient C_p/C_{p0} and the blade structural compliance c/c_0 monotonically increase with increasing weighting factor ω. The rotor power coefficient of the NREL 5 MW wind turbine rotor, used here as a reference model from which the optimization simulations are initiated, equals $C_p = C_{p0} = 0.459$. As illustrated in Fig. 16, this value indeed is representative of the two simulations in which the power coefficient is left out of consideration in the optimization procedure, i.e., the pure STO approach and the CMSTO approach with $\omega = 0$. Note that the normalized structural compliance c/c_0 is different for these two cases, since in the CMSTO approach the structural compliance is dependent on *both* the shape and topology design variables, $c = c(\mathbf{a}, \boldsymbol{\rho})$, see Eq. (1), whereas in the STO approach it only depends on the topology variables, $c = c(\boldsymbol{\rho})$, see Eq. (5). By increasing the weighting factor from $\omega = 0$ to $\omega = 0.75$, the power coefficient grows from 0.459 to 0.479, which

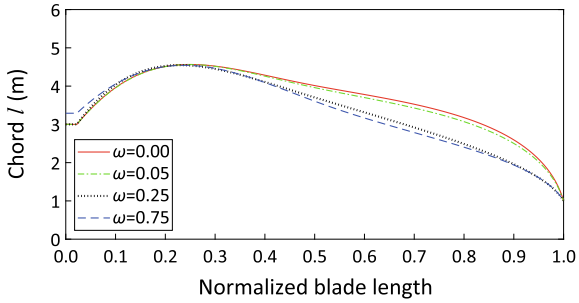

Fig. 17. Optimized blade chord distribution calculated with the CMSTO approach using different weighting factors ω.

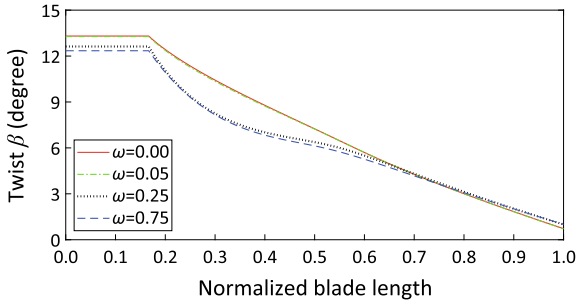

Fig. 18. Optimized blade twist distribution calculated with the CMSTO approach using different weighting factors ω.

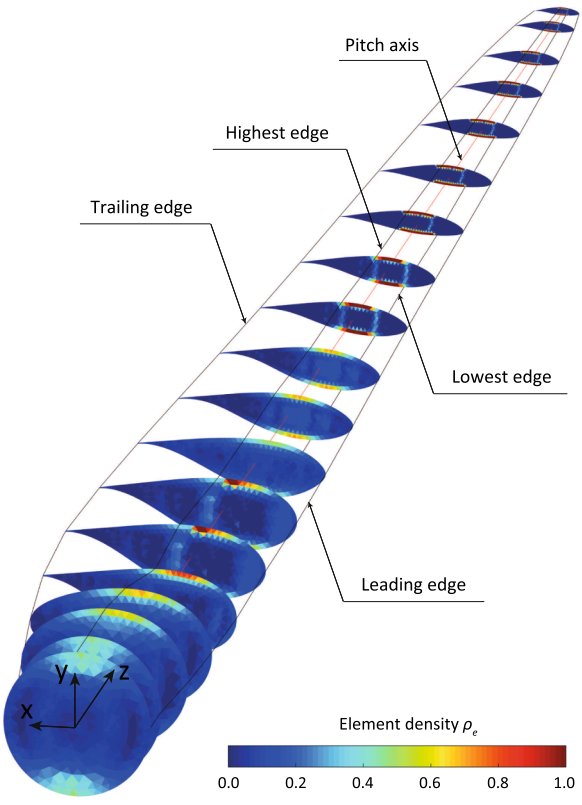

Fig. 19. Optimized blade geometry and internal topology calculated with CMSTO using a weighting factor $\omega = 0.75$.

corresponds to an increase of 4%. Hence, it may be concluded that the shape of the NREL 5 MW reference blade already is close to optimal from an aerodynamical viewpoint. Note further that an increase of the weighting factor from $\omega = 0$ to $\omega = 0.75$ leads to an increase of the blade structural compliance of approximately a factor of 2, which

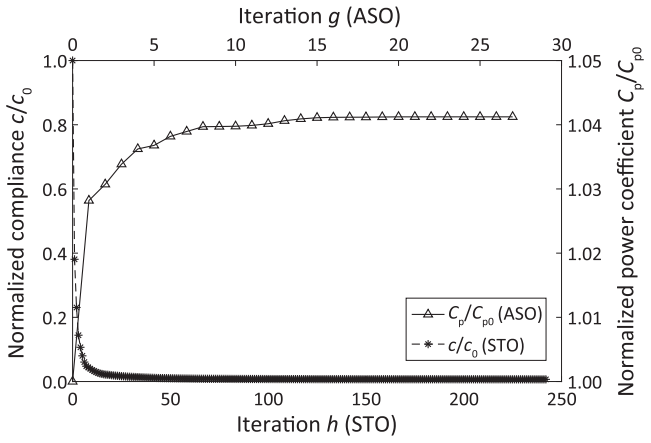

Fig. 20. Convergence behavior of the normalized power coefficient C_p/C_{p0} and normalized compliance c/c_0, using the separate ASO-STO approach.

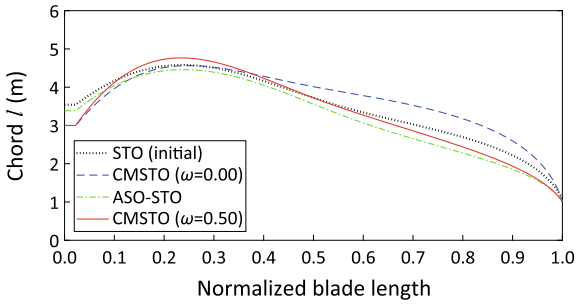

Fig. 21. Optimized blade chord distribution calculated with the ASO-STO approach and the CMSTO approach with $\omega = 0.50$.

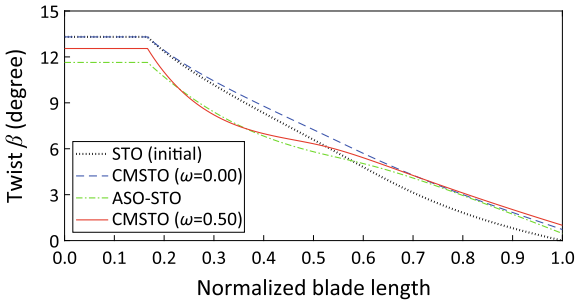

Fig. 22. Optimized blade twist distribution calculated with the ASO-STO approach and the CMSTO approach with $\omega = 0.50$.

obviously is disadvantageous. In summary, an increase of the power coefficient goes at the expense of an increase in blade compliance (and thus a decrease in blade stiffness), whereby the specific design requirements of the turbine blade determine how these two aspects should be weighted in the optimization process, using a weighting factor within the range of the APF, $0 \leqslant \omega \leqslant 0.75$.

The effect of the blade geometry on the aerostructural performance can be examined in more detail by considering the chord and twist distributions of the optimized designs, calculated by CMSTO with $\omega = 0, 0.05, 0.25, 0.75$, see Figs. 17 and 18, respectively. It is observed from Fig. 17 that for a decreasing weighting factor ω the blade chord length – and also the blade thickness, given the fact that the specific blade cross-section is constant – over a significant part of the blade length becomes larger, which indeed enlarges the overall blade stiffness, see also Fig. 16. In addition, Fig. 18 shows that along the first half length of the blade a higher weighting factor ω leads to a decrease in the blade twist angle β. Consequently, the angle of attack, $\alpha = \phi - \beta$, of the

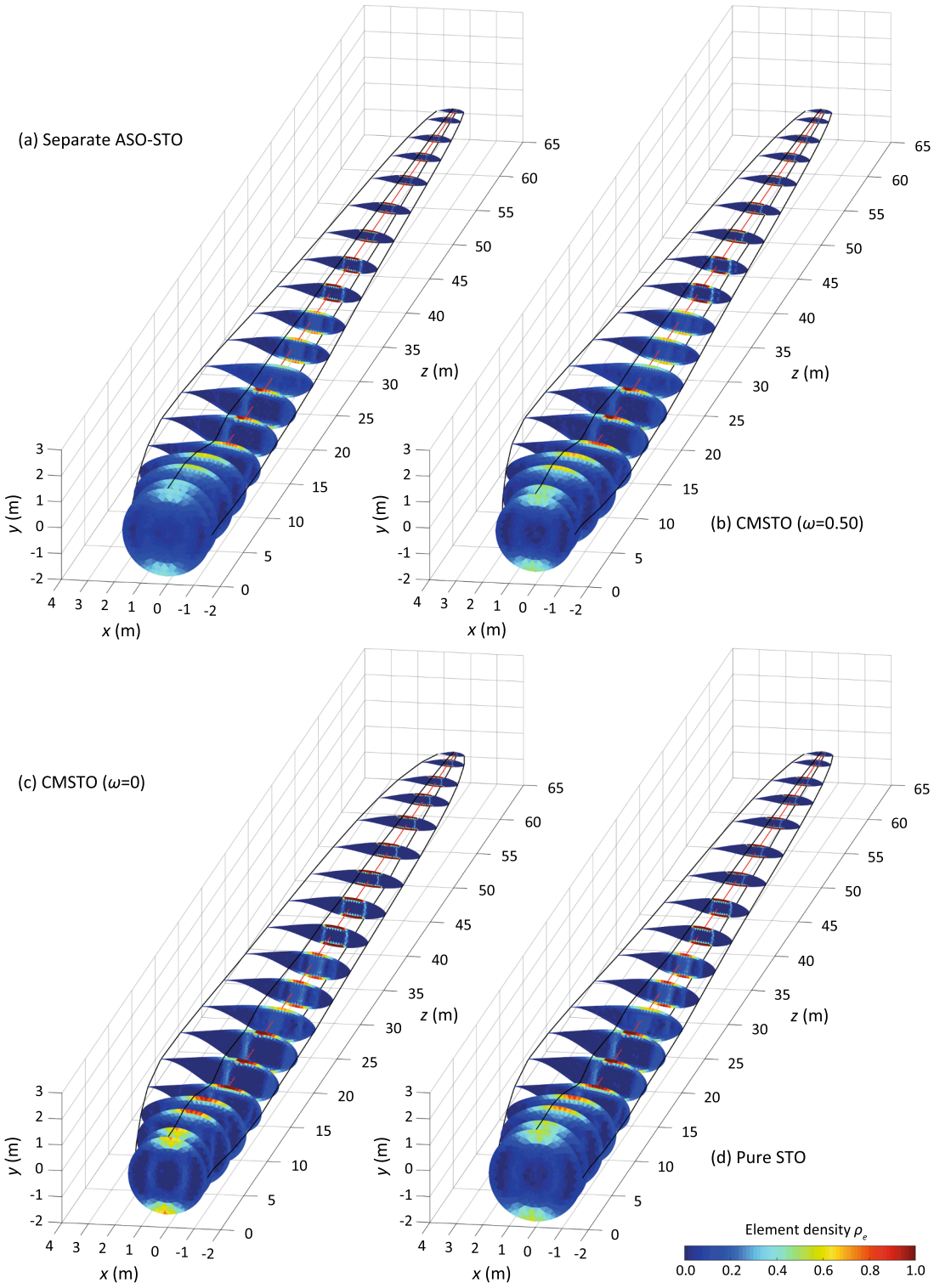

Fig. 23. Optimized blade geometry and internal topology calculated by (a) the separate ASO-STO approach, (b) the CMSTO approach with $\omega = 0.50$, (c) the CMSTO approach with $\omega = 0$ and (d) the pure STO approach.

blade cross-section increases, which – before reaching dynamic stall [14] – results in a higher lift coefficient, and thus in a higher rotor power output, as in agreement with the trend observed in Fig. 16.

Fig. 19 shows the optimized outer shape of the blade and the internal topology at various blade cross-sections along the blade length, as computed by the CMSTO approach for a weighting factor $\omega = 0.75$. It can be observed that for each cross-section two spar caps are found. Furthermore, some cross-sections located between the half length and the tip of the turbine blade are characterized by the presence of two shear webs. Although such a topology indeed bears similarities with conventional blade layout designs [8], the specific size and location of the spar caps and shear webs are optimized in this analysis.

The separate ASO-STO approach often used in blade design practice is also able to optimize both the blade outer shape and the interior layout, but does this in two consecutive steps. Specifically, first the blade outer shape is optimized by maximizing the normalized power

coefficient C_p/C_{p0} in accordance with Eq. (4), whereby the weight factor equals unity, $\omega = 1$. Subsequently, with the obtained blade outer shape and corresponding aerodynamic loads, the interior topology of the blade is optimized by minimizing the structural compliance c/c_0, setting $\omega = 0$ in Eq. (5). The convergence behavior of the ASO-STO approach is shown in Fig. 20, by plotting the objectives C_p/C_{p0} and c/c_0 of the ASO and STO steps as a function of the corresponding number of iterations g and h, respectively. The figure clearly shows that the number of iterations for the ASO step is almost an order of magnitude lower than for the STO step. The optimized result computed with the ASO-STO approach is depicted in Fig. 16 using an asterisk symbol. Interestingly, the structural compliance of the blade design following from the ASO-STO approach is higher than that of the CMSTO designs presented, and thus less optimal. On the contrary, the ASO-STO design corresponds to a similarly high power coefficient as found for the CMSTO designs with weighting factors ranging between $0.25 \leqslant \omega \leqslant 0.99$; this is obviously due to the fact that in the ASO-STO approach the aerodynamic optimization step is performed first, and that during the subsequent topology optimization step only the interior blade layout is allowed to change.

In Figs. 21 and 22 the chord and twist distributions of the blade designs computed with the CMSTO approach for $\omega = 0$ and 0.50 are compared to the distributions calculated by the STO and ASO-STO approaches. The two weighting factors considered here in the CMSTO approach correspond to typical design situations: $\omega = 0$ refers to the minimization of the blade structural compliance only, while $\omega = 0.5$ reflects that minimizing the blade structural compliance and maximizing the rotor power coefficient are equally important. Note that in the design practice the choice of the weighting factor generally is determined by specific design conditions and requirements. Fig. 21 shows that for a large part of the blade length the chord length obtained by the CMSTO approach with $\omega = 0$ is considerably larger than for the three other cases, which is in correspondence with a significantly higher blade stiffness, see Fig. 16. In addition, Fig. 22 indicates that along the first half length of the blade the CMSTO approach with $\omega = 0$ and the STO approach result in a larger twist angle than the CMSTO approach with $\omega = 0.50$ and the ASO-STO approach, which, as explained above, translates into a lower rotor power coefficient, see Fig. 16. The above features can be also observed from the optimized geometries of the four cases, see Fig. 23. The internal topological layouts of the four cases globally look comparable, but differ by the precise locations and dimensions of the spar caps and shear webs.

The use of a gradient-based optimization approach, together with the Blade Element Momentum method, has made it possible to optimize the three-dimensional rotor blade geometry in a computationally efficient way. Although the use of gradient-free optimization algorithms, such as genetic algorithms [2–7,25,26], allows for a more easy numerical implementation and the possibility of finding a global optimum, these algorithms are known to be computationally expensive for density-based topology optimization [43]. This is especially the case when considering large structures, such as wind turbine blades, which makes them less suitable for these applications.

5. Conclusions

A coupled multi-objective shape and topology optimization (CMSTO) framework has been proposed for the aerostructural design of HAWT rotor blades. The framework enables to simultaneously optimize the outer shape and the internal structural layout of the turbine blade with respect to aerodynamic and structural requirements. The optimization process is performed on the weighted sum of two design objectives, which are the rotor power coefficient and the structural compliance of the blade. The power coefficient and structural compliance are evaluated in a computationally efficient manner by using so-called BEM and beam FEM models, respectively. The shape design variables are represented by the locations of NURBS control points that govern the blade geometry. The topology design variables are represented by the relative densities assigned to the finite elements modeling the blade cross-sections, in accordance with the SIMP method. The coupled optimization model for a turbine blade is solved in an incremental-iterative fashion, by alternatively performing shape and topology optimization steps, until the solution satisfies the convergence criterion imposed. Here, the computational efficiency of the numerical procedure is warranted through the use of closed-form sensitivities in a gradient-based algorithm for the CMSTO approach.

The specific features of the CMSTO approach are demonstrated by comparing the optimized design computed for a NREL 5 MW reference rotor blade with the results obtained from a separate ASO-STO approach and a pure STO approach. The optimization results following from the CMSTO approach for different weighting factors indicate that the overall stiffness of a blade typically decreases with an increase of the rotor power coefficient. The rotor power coefficients of the designs generated by the CMSTO approach with a weighting factor $\omega = 0.75$ and the ASO-STO approach are about 4% larger than that of the reference rotor blade. However, the structural compliance of the blade calculated by the CMSTO approach with $\omega = 0.75$ is 16% lower than that computed by ASO-STO approach. The application of the CMSTO approach with the aerodynamic optimization being switched off leads to a reduction of the blade structural compliance of approximately 41% compared to a pure STO approach. Such significant improvements clearly demonstrate the benefits of the CMSTO approach in the quest of wind turbines with higher power output and better structural performance.

In order to validate the optimized rotor blade geometries computed in this work, more systematic experimental studies are necessary, both in regards to the shape and topology designs of blade structures. This is a topic for future study.

CRediT authorship contribution statement

Zhijun Wang: Methodology, Formal analysis, Writing - original draft. **Akke S.J. Suiker:** Methodology, Supervision, Writing - original draft. **Hèrm Hofmeyer:** Methodology, Supervision, Writing - original draft. **Twan van Hooff**: Supervision, Writing - review & editing. **Bert Blocken:** Supervision, Writing - review & editing.

Declaration of Competing Interest

The authors declare that they have no known competing financial interests or personal relationships that could have appeared to influence the work reported in this paper.

Acknowledgements

The financial support of Z.W. by the China Scholarship Council (CSC) is gratefully acknowledged. Z.W. is grateful to the National Renewable Energy Laboratory (NREL), Colorado, United States for providing the open source software CCBlade. The authors gratefully acknowledge the supercomputer facilities provided by the NWO Exacte Wetenschappen (Physical Sciences). T.v.H. currently is a postdoctoral fellow of the Research Foundation – Flanders (FWO) and acknowledges its financial support (project FWO 12R9718N).

References

[1] Chehouri A, Younes R, Ilinca A, Perron J. Review of performance optimization techniques applied to wind turbines. Appl Energy 2015;142:361–88.
[2] Wang L, Wang T, Wu J, Chen G. Multi-objective differential evolution optimization based on uniform decomposition for wind turbine blade design. Energy 2017;120:346–61.
[3] Neto JXV, Junior EJG, Moreno SR, Ayala HVH, Mariani VC, dos Santos Coelho L. Wind turbine blade geometry design based on multi-objective optimization using metaheuristics. Energy 2018;162:645–58.

[4] Shen X, Chen J-G, Zhu X-C, Liu P-Y, Du Z-H. Multi-objective optimization of wind turbine blades using lifting surface method. Energy 2015;90:1111–21.
[5] Dal Monte A, De Betta S, Castelli MR, Benini E. Proposal for a coupled aerodynamic–structural wind turbine blade optimization. Compos Struct 2017;159:144–56.
[6] Dal Monte A, Castelli MR, Benini E. Multi-objective structural optimization of a HAWT composite blade. Compos Struct 2013;106:362–73.
[7] Fagan EM, De La Torre O, Leen SB, Goggins J. Validation of the multi-objective structural optimisation of a composite wind turbine blade. Compos Struct 2018;204:567–77.
[8] Burton T, Jenkins N, Sharpe D, Bossanyi E. Wind energy handbook. John Wiley & Sons; 2011.
[9] Zhu WJ, Shen WZ, Sørensen JN. Integrated airfoil and blade design method for large wind turbines. Renew Energy 2014;70:172–83.
[10] Shen X, Yang H, Chen J, Zhu X, Du Z. Aerodynamic shape optimization of non-straight small wind turbine blades. Energy Convers Manage 2016;119:266–78.
[11] Vučina D, Marinić-Kragić I, Milas Z. Numerical models for robust shape optimization of wind turbine blades. Renew Energy 2016;87:849–62.
[12] Tahani M, Kavari G, Masdari M, Mirhosseini M. Aerodynamic design of horizontal axis wind turbine with innovative local linearization of chord and twist distributions. Energy 2017;131:78–91.
[13] Hansen MOL, Sørensen JN, Voutsinas S, Sørensen N, Aa H. Madsen, State of the art in wind turbine aerodynamics and aeroelasticity. Prog Aerospace Sci 2006;42(4):285–330.
[14] Geng F, Kalkman I, Suiker ASJ, Blocken B. Sensitivity analysis of airfoil aerodynamics during pitching motion at a Reynolds number of 1.35×10^5. J Wind Eng Ind Aerodyn 2018;183:315–32.
[15] Rezaeiha A, Montazeri H, Blocken B. Characterization of aerodynamic performance of vertical axis wind turbines: Impact of operational parameters. Energy Convers Manage 2018;169:45–77.
[16] Rezaeiha A, Montazeri H, Blocken B. Towards optimal aerodynamic design of vertical axis wind turbines: Impact of solidity and number of blades. Energy 2018;165:1129–48.
[17] Bak C. Aerodynamic design of wind turbine rotors. Advances in wind turbine blade design and materials. Elsevier; 2013. p. 59–108.
[18] Jensen FM, Branner K. Introduction to wind turbine blade design. Advances in wind turbine blade design and materials. Elsevier; 2013. p. 3–28.
[19] Bottasso CL, Campagnolo F, Croce A, Dilli S, Gualdoni F, Nielsen MB. Structural optimization of wind turbine rotor blades by multilevel sectional/multibody/3D-FEM analysis. Multibody Syst Dyn 2014;32(1):87–116.
[20] Barnes RH, Morozov EV. Structural optimisation of composite wind turbine blade structures with variations of internal geometry configuration. Compos Struct 2016;152:158–67.
[21] Sjølund JH, Lund E. Structural gradient based sizing optimization of wind turbine blades with fixed outer geometry. Compos Struct 2018;203:725–39.
[22] Buckney N, Green S, Pirrera A, Weaver PM. On the structural topology of wind turbine blades. Wind Energy 2013;16(4):545–60.
[23] Pavese C, Tibaldi C, Zahle F, Kim T. Aeroelastic multidisciplinary design optimization of a swept wind turbine blade. Wind Energy 2017;20(12):1941–53.
[24] Barrett R, Ning A. Integrated free-form method for aerostructural optimization of wind turbine blades. Wind Energy 2018;21(8):663–75.
[25] Pourrajabian A, Afshar PAN, Ahmadizadeh M, Wood D. Aero-structural design and optimization of a small wind turbine blade. Renew Energy 2016;87:837–48.
[26] Yang H, Chen J, Pang X, Chen G. A new aero-structural optimization method for wind turbine blades used in low wind speed areas. Compos Struct 2019;207:446–59.
[27] Ning A, Petch D. Integrated design of downwind land-based wind turbines using analytic gradients. Wind Energy 2016;19(12):2137–52.
[28] Marler RT, Arora JS. Survey of multi-objective optimization methods for engineering. Struct Multidiscip Optim 2004;26(6):369–95.
[29] Blasques JP, Bitsche RD, Fedorov V, Lazarov BS. Accuracy of an efficient framework for structural analysis of wind turbine blades. Wind Energy 2016;19(9):1603–21.
[30] Wang Z, Suiker ASJ, Hofmeyer H, van Hooff T, Blocken B. Sequentially coupled shape and topology optimization for 2.5D and 3D beam-type structures. Submitted.
[31] Piegl L, Tiller W. The NURBS book. Berlin: Springer; 1995.
[32] Ning SA. CCBlade [Tech. Rep.]. Golden, CO (United States): National Renewable Energy Laboratory (NREL); 2013.
[33] Wang Z, Suiker ASJ, Hofmeyer H, Kalkman I, Blocken B. Sequentially coupled gradient-based topology and domain shape optimization. Submitted.
[34] Bendsøe MP, Sigmund O. Topology optimization: theory, methods and applications. Berlin: Springer; 2003.
[35] Jonkman J, Butterfield S, Musial W, Scott G. Definition of a 5-MW reference wind turbine for offshore system development [Technical Report No. NREL/TP-500-38060]. National Renewable Energy Laboratory, Golden, CO.
[36] Resor BR. Definition of a 5MW/61.5 m wind turbine blade reference model. Sandia National Laboratories: Albuquerque, New Mexico, USA; 2013. SAND2013-2569.
[37] Takizawa K, Henicke B, Tezduyar TE, Hsu M-C, Bazilevs Y. Stabilized space-time computation of wind-turbine rotor aerodynamics. Comput Mech 2011;48(3):333–44.
[38] Ning SA. A simple solution method for the blade element momentum equations with guaranteed convergence. Wind Energy 2014;17(9):1327–45.
[39] Rommel DP, Di Maio D, Tinga T. Calculating wind turbine component loads for improved life prediction. Renew Energy 2020;146:223–41.
[40] Hansen MOL. Aerodynamics of wind turbines. Earthscan; 2008.
[41] Sigmund O. A 99 line topology optimization code written in Matlab. Struct Multidiscip Optim 2001;21(2):120–7.
[42] Emmerich MTM, Deutz AH. A tutorial on multiobjective optimization: fundamentals and evolutionary methods. Natural Comput 2018;17(3):585–609.
[43] Sigmund O. On the usefulness of non-gradient approaches in topology optimization. Struct Multidiscip Optim 2011;43(5):589–96.